Factors limiting contrail detection in satellite imagery

Oliver G. A. Driver[1], Marc E. J. Stettler[2], and Edward Gryspeerdt[1,3]

[1]Department of Physics, Imperial College London, London, United Kingdom
[2]Department of Civil and Environmental Engineering, Imperial College London, London, United Kingdom
[3]Grantham Institute - Climate Change and the Environment, Imperial College London, London, United Kingdom

Correspondence: Oliver G. A. Driver (o.driver22@imperial.ac.uk)

Abstract. Contrails (clouds produced by aircraft exhaust) have a significant warming contribution to the overall climate impact of aviation. This makes reducing them a key target for future climate strategies in the sector. Identifying pathways for contrail reduction requires accurate models of contrail formation and lifecycle, which in turn need suitable observations to constrain them. Infrared imagers on geostationary satellites provide widespread, time-resolved observations of the evolution of contrail properties. However, contrails are often narrow and optically thin, which makes them challenging for satellites to identify. Quantifying the impact of contrail properties on observability is essential to determine the extent to which satellite observations can be used to constrain contrail models and to assess the climate impact of aviation.

In this work, contrail observability is tested by applying a simple contrail detection algorithm to synthetic images of contrails in an otherwise-clear sky against a homogeneous ocean background. Only (46 ± 2) % of a modelled population of global contrail segments are found to be observable using current 2 km resolution instruments, even in this maximally-observable case. A significantly higher portion of contrail forcing is detectable using the same imager—(82 ± 2) % of instantaneous longwave forcing—because observable contrails have a larger climate impact. This detection efficiency could be partly improved by using a higher-resolution infrared imager, which would also allow contrails to be detected earlier in their lifecycle. However, even this instrument would still miss the large fraction of contrails that are too optically thin to be detected.

These results support the use of contrail detection and lifetime observations from existing satellite imagers to draw conclusions about the relative radiative importance of different contrails under near-ideal conditions. However, there is a highlighted need to assess the observability of specific contrails depending on the observation requirements of a given application. These observability factors are shown to change in response to climate action, demonstrating a need to consider the properties of the observing system when assessing the impacts of proposed mitigation strategies.

1 Introduction

Contrail cirrus is recognised as a significant driver of aviation's climate warming: Lee et al. (2021) suggest it is the cause of more than half the radiative forcing of the sector. Contrail forcing is warming in the longwave (LW), via the cloud greenhouse effect, and cooling in the shortwave (SW), via the cloud albedo effect (Meerkötter et al., 1999). This strong anthropogenic radiative forcing provides impetus for action on contrail mitigation and research.

25   Early estimates of the radiative forcing due to contrails (e.g. Meerkötter et al., 1999; Meyer et al., 2002) relied on the scaling of radiative transfer simulations to the coverage of linear contrails—measured regionally in satellite observations via manual identification (Bakan et al., 1994) or algorithms for detecting line-shaped ice clouds (Mannstein et al., 1999). The observations use infrared images—particularly split-window brightness temperature images (Lee, 1989) which highlight optically thin ice clouds with small crystals against the surface and background liquid clouds. Historically, geostationary satellites did not offer

30   high-enough spatial resolution to detect contrails, as illustrated by the use of imagers on low-Earth orbiting (LEO) satellites for contrail detection (Mannstein et al., 1999; Duda et al., 2013; Vázquez-Navarro et al., 2015). Geostationary observations have the advantage of continuous observation of the same scene with a single instrument, sufficiently time-resolved to observe contrail evolution. Some studies, including Vázquez-Navarro et al. (2015), have identified contrails in LEO satellite imagery before tracking them in geostationary images. Some contrails were only observable in LEO imagery, demonstrating an instru-

35   ment dependence of observablity. Gierens and Vázquez-Navarro (2018) used statistical approximations to derive that contrails tracked using this technique may be observable for less than half their lifetime, considering unobserved parts of the evolution both before and after observation. Several recent observational studies have demonstrated the ability to detect contrails using modern geostationary satellites (GOES-R series and Himawari 8), including Zhang et al. (2018); Meijer et al. (2022); Ng et al. (2023). This treatment neglects to consider the contrails which remain unobservable by human labellers. These modern

40   satellites have infrared bands used for contrail detection with approximately 2 km resolution at nadir. Initial detection in geostationary images has been found to occur 10–30 minutes after formation (Chevallier et al., 2023; Gryspeerdt et al., 2024), indicating that contrails are unobservable for at least the earlier part of their evolution.

Kärcher et al. (2009) established that simulated and observed distributions of contrail optical thicknesses differ, and can be reconciled using optical-thickness-dependent detection efficiencies. Previously, studies had focused on relative detection

45   efficiency due to surface inhomigeneities and overdetections due to false positives (Mannstein et al., 1999; Meyer et al., 2002; Minnis et al., 2005; Palikonda et al., 2005; Meyer et al., 2007). The Kärcher et al. (2009) approach goes some way to enabling estimates of contrail coverage which align more closely with model output, albeit with detection efficiency inferred empirically based on the population simulated by the model. It is also clear that contrail detectability depends not only on the optical thickness of a contrail, but also the microphysical properties (Yang et al., 2010). Increasingly-prevelant convolutional

50   neural net algorithms are typically benchmarked against human-identifiable contrails used as training data (Meijer et al., 2022; Ng et al., 2023; Gryspeerdt et al., 2024). If these satellite-observed contrails are to be used to evaluate model simulations on contrails, it is essential that the properties of the observing system are taken into account—a concept known as "satellite simulation" (e.g. Bodas-Salcedo et al., 2011). With varying instrument properties and a wide variety of contrail micro and macrophysical properties, it is not clear that a simple optical depth threshold is suitable for this purpose.

55   Validation of models, like CoCiP (the 'Contrail Cirrus Prediction model'; Schumann, 2012) requires well-understood observations. CoCiP produces predictions which align with observations, insofar as their properties are resolved (Schumann et al., 2017). CoCiP predictions have been used for predicting contrail formation in order to guide in-situ observations (Voigt et al., 2017). CoCiP has also been used to consider potential consequences of lower non-volatile particulate emissions following climate action, such as due to the adoption of Sustainable Aviation Fuel (SAF) (Teoh et al., 2022b). CoCiP is based on sim-

60 ple, well-understood criteria for formation and persistence, described in Schumann (1996). Most fundamentally, this is driven by Schmidt–Appleman temperature threshold for mixing cloud formation and ice-supersaturation conditions for persistence (with appropriate adaptations, for example, for propulsion efficiency). Meteorological input limits the predictability of contrail formation, particularly uncertainty in relative humidity values at flight altitudes (Gierens et al., 2020; Agarwal et al., 2022). Model adaptations, such as the correction of relative humidity measurements (Teoh et al., 2022a) or alterations to ice crystal

65 formation and loss mechanisms (Schumann et al., 2017), require well-understood contrail observations for validation.

Beyond model validation, other applications have a varied range of observational needs. Climate monitoring and tactical avoidance applications (Geraedts et al., 2023; Chevallier et al., 2023; Sausen et al., 2023) require observation of as high a proportion of strongly forcing contrails as possible (and at least at some point in their evolution). The same applications need to match contrails to flights and dynamically avoid contrails, so observation as quickly after formation as possible is required.

70 Avoidance trials benefit from an understanding of the dependence of observability on the properties of contrails, so that they can be confident that unobserved contrails are indeed unformed contrails (Molloy et al., 2022).

This study establishes limits of contrail observability as a function of the contrail properties independently from models. Contrail detection is simulated in otherwise-clear-sky synthetic radiance fields, by applying a contrail detection algorithm that reflects the contrails visible in-context. The derived observability threshold will then be compared with a baseline contrail

75 population and its estimated radiative forcing, and the consequences for a range of applications will be considered. In Section 2.1, the simulated contrail images are described, including radiative transfer simulations used to model them. These images are tested using the line-filtering detection algorithm described in Section 2.2. A modelled population of contrails, detailed in Section 2.3, is used to consider the consequences of derived observability thresholds. Observability assessments are made in Section 3, including varying single parameters (Section 3.1) and derivation of an observability threshold against the key

80 observability-driving properties (Section 3.2)—properties which form a parameter space in which the population of contrails is shown to be well-resolved (Section 3.3). The resulting proportion of contrails and contrail forcing that can be observed are found (Section 4.1), as well as the evolution of this observability with contrail aging (Section 4.2). The validity of radiative importance conclusions made from the observed lifetime is scrutinised in Section 4.3, followed by a consideration of the changing observability as climate action is taken (Section 4.4)

2 Algorithms and data

2.1 Simulated contrail images

The observability of a contrail segment is tested by running a contrail detection algorithm (Section 2.2) over simple simulated radiance fields of synthetic straight-line contrails above a clear-sky ocean scene. The process is outlined in the schematic, Fig. 1, and described below.
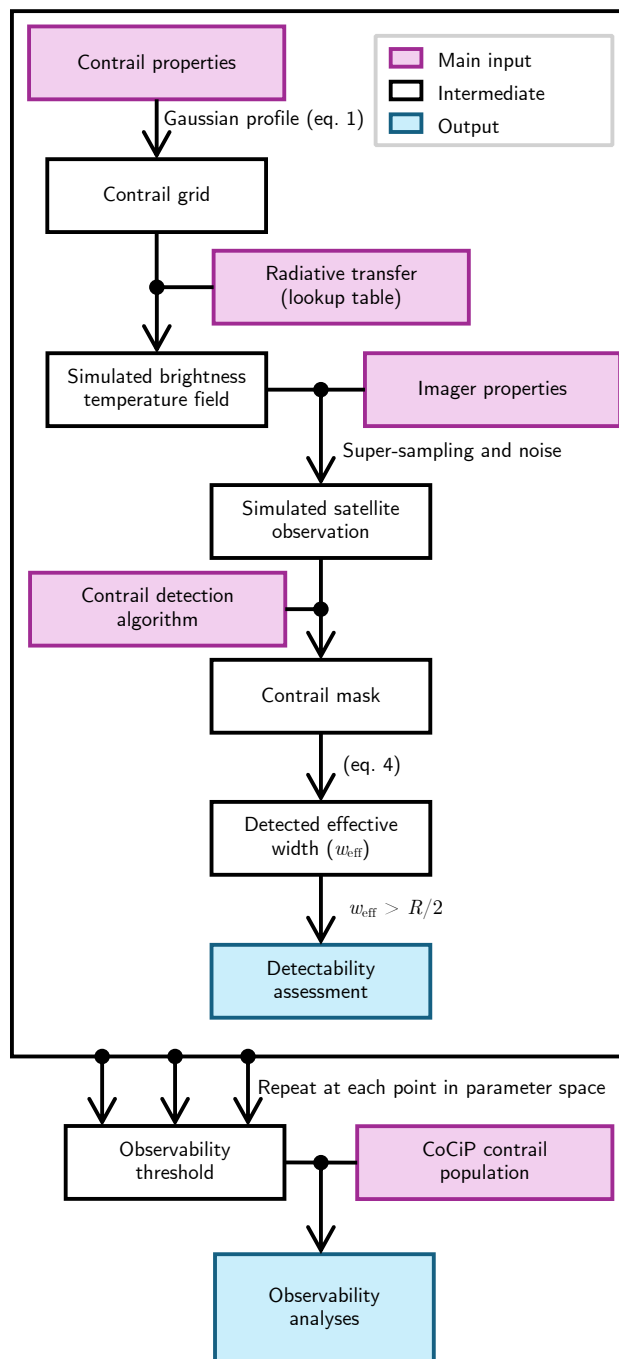
Figure 1. The process for deriving the probability of observation detected by repeated application of a contrail detection algorithm to synthetic observations of a single contrail, using a specified imager, detection algorithm, and calculated radiative transfer lookup table.
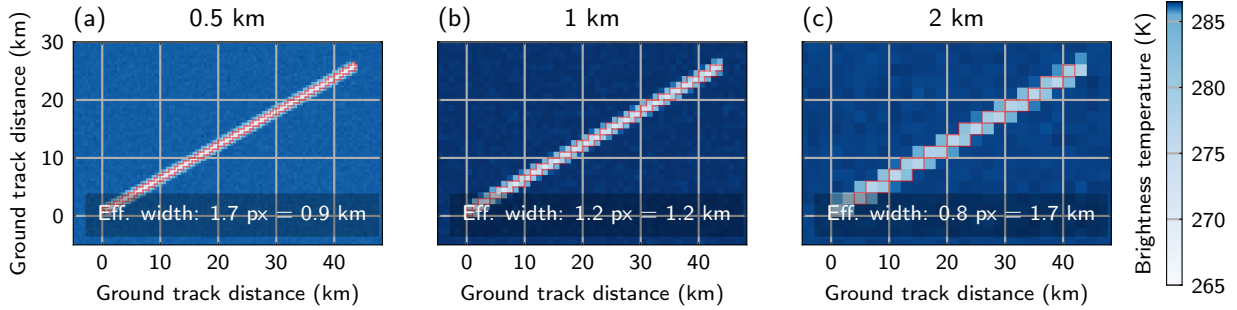
Figure 2. Example simulated contrails used for theoretical observability testing. Red line denotes the contrail mask detected. Note the skewed colour scheme intended to simultaneously highlight imager noise and decreased peak brightness temperature with the coarsening resolution. Image-to-image variability is given by a simulated calibration error, and pixel-to-pixel by the NEdT.

Test contrails are constructed as 50 km long cloud segments, with an ice water path (IWP) varied across the contrail in a Gaussian profile. The profile has the form

$$\mathrm{IWP}(s;\ \mathrm{IWP}_0,\ B) = \mathrm{IWP}_0\ \sqrt{\frac{4}{\pi}}\exp\left(-\frac{1}{2}\frac{s^2}{B^2/8}\right), \tag{1}$$

describing variations from the contrail IWP (IWP_0) across the distance perpendicular to the contrail's length (s), given the width of the specific test contrail (B). This is consistent with the optical depth profile used for CoCiP-modelled contrails, described in Schumann (2012). A 1-D radiative transfer simulation using the US standard atmosphere is run at each point in the test contrail, on a 0.25 km grid, to produce a radiance field (at 'high-resolution' relative to satellite imager output), from which brightness temperatures are calculated. The DISORT algorithm (Buras et al., 2011) was used for radiative transfer calculations, as implemented in the libRadtran library (Emde et al., 2016), with the pyLRT python wrapper (Gryspeerdt and Driver, 2024) used to perform the simulations. The ice water content and droplet size distribution are assumed uniform across the contrail depth. When $r_{\mathrm{eff}} > 5\ \mu\mathrm{m}$, the contrails are parameterised using the Yang et al. (2013) parameterisation as distributed with libRadtran, using smooth droxtal (faceted spheroid) habits. The lower-limit on r_{eff} is a limit of this parameterisation. To simulate contrails with smaller ice crystals, absorption coefficients were calculated using the 'mie' package (also distributed with libRadtran) for spherical ice crystals with a Gamma distribution of particle radii consistent with the libRadtran microphysics implementation. GOES-ABI imager bands are simulated using the REPTRAN representative wavelength parameterisation (Gasteiger et al., 2014). Additional radiative transfer simulations are made of contrails against a layer of cirrus background, as well as the baseline sythetic observations which are made in otherwise-clear sky. The background cirrus layer is 500 m deep, at 8 km altitude, with an effective radius of 5 μm (chosen as the intersection of the two ice cloud parameterisations due technical limitations) and IWP of 25 gm^{-2}. The layer has an optical thickness of approximately 3.

For computational efficiency, a lookup table of brightness temperature values for a comprehensive range of contrail physical properties was used to produce the simulated brightness temperature fields. The radiative transfer lookup table is based in a parameter space grid, linearly-spaced in IWP (between 0 and 100 g m^{-2}), r_{eff} (between 0.1 and 80 μm), contrail depth (between

50 and 1500 m), and altitude (between 6 and 13 km). Linear spacing of the lookup table includes more gradual variations in simulated radiances than a lograrithmically spaced parameter grid, so is better suited for interpolation where required.

The high-resolution simulated brightness temperature field is then processed to simulate the properties of a given imager,
115 coarsening the resolution and applying measurement noise. The brightness temperature grid is coarsened to a grid given by the imager's resolution, using a conservative local-mean downgridding technique (to integer multiples of the high resolution grid). A Gaussian noise with standard deviation equal to a noise-equivalent temperature deviation (NEdT) of 0.03 K is applied to simulate the pixel-to-pixel uncertainty—approximately equivalent to the GOES-ABI NEdT based on on-orbit tests of GOES-16 (NOAA, 2019; Wu and Schmidt, 2019). Multiple realisations of the brightness temperature field are produced, each offset
120 with a single calibration error sampled for a 0.2 K—representative of the image-to-image uncertainty of the GOES-ABI imager (NOAA, 2019). Fig. 2 shows simulated brightness temperature fields for the GOES-ABI band 14 (centred on 11.2 μm) for a range of resolutions.

2.2 Contrail detection algorithm and observability criteria

A simple convolutional filtering contrail detection algorithm is applied to the images. The detection algorithm used is based on
125 the implementation of the Mannstein et al. (1999) algorithm distributed with McCloskey et al. (2021). This is a line-filtering algorithm, applied on infrared brightness temperature fields. Brightness temperature (using the 11.2 μm band of the GOES ABI instrument) and brightness temperature difference (between the 10.3 and 12.3 μm bands of the same instrument) fields are used for contrail detection. The fields are lowpass-filtered, differenced from a smoothed version to extract the signal, normalised, and clipped of extreme values. A threshold is applied to each of the two fields, as well as a combined field convolved with
130 line filters in a range of different directions. For the McCloskey et al. (2021) implementation, the thresholds have been tuned on a human-labelled dataset, establishing the contrails detected using this algorithm as representative of those observable by human labellers. The change resulting from altering these thresholds to detect contrails producing a minimally-detectable signal against imager noise are briefly considered in Section 4.1, although this would require controls to mitigate the risk of false positive detections in real observations (e.g. targeted observation of a specific contrail).

135 The algorithm has been minimally adapted in this work to relieve some emergent issues. The algorithm was found to selectively omit contrails aligned with the dimensions of the simulated imager grid, a result of using the r-squared statistic as a test for linearity. A linearity score was devised to replace the r-squared statistic,

$$\epsilon^2 = 1 - \frac{\sum d_\perp^2}{\sum d_\parallel^2}, \tag{2}$$

where $d_\perp$ is the perpendicular distance to a pixel from a linear fit to the masked points, and $d_\parallel$ the distance between a masked
140 pixel and the midpoint of the line, and sums act over each of the pixels in the detected area. ϵ is the eccentricity of an ellipse whose semi-major and semi-minor axes are the mean $d_\parallel$ and $d_\perp$ respectively. This relieves the dependence on axes arbitrarily chosen relative to the contrail.

Detected contrails were also checked for their alignment with the simulated contrail. Regions whose orientation differed from the simulated contrail by $\pm\ 30°$ are neglected. This removes artefacts where the 'end' of the contrail has been detected, but

145 not the main body of the contrail. This is a result of the contrail profiles terminating suddenly, producing a regional gradient in brightness temperature fields, highlighted by the Mannstein et al. (1999) style detector. This only arises for very wide, optically thick simulated contrails, it is not a measure that would ever be required for operational contrail detection of physically realistic contrails.

The algorithm produces a mask of contrail pixels from an image, of area

$$A_\text{mask} = N_\text{px} R^2, \tag{3}$$

where N_px is the number of masked pixels and R the imager resolution. The presence of a contrail has been accurately detected if the mask is made up of at least one pixel along the length of the contrail. It is useful to consider the width of the area detected as a contrail, because an imager is only able to detect an area in units of pixels. We define the 'effective width' as

$$w_\text{eff} = \frac{A_\text{mask}}{l} \Rightarrow \frac{w_\text{eff}}{R} = \frac{N_\text{px}}{l/R}. \tag{4}$$

155 A one-pixel effective width ($w_\text{eff} = R$) corresponds to a minimally detected contrail along the whole length of the contrail. For each simulated contrail detection attempt, a threshold $w_\text{eff} > R/2$ is applied, such that a detection along most of the length, but not neccessarily all, is accepted. This minimally-restrictive condition ensures that very narrow contrails whose ends are omitted from the mask are not penalised as failed detections. Observability is tested against this condition using four different realisations of the instrument noise, before aggregating the probability of detection (P_obs) for a particular set of cloud properties.

160 An 'observability threshold' is then determined in the parameter space, for contrails with $P_\text{obs} > 0.5$. P_obs thresholds of 0.25 (detected in one realisation) and 0.75 (detected in all but one realisation) are used to indicate the uncertainty in the observability threshold. This is only a small contribution to the uncertainty in later-derived fractions of observable contrails compared to seasonal and diurnal variability in the properties of the contrails in the population and their estimated radiative forcing.

2.3 The distribution of "real" contrail properties

165 A baseline population of contrails and their properties is needed to analyse whether the most climatically relevant contrails are observable: those which form and persist, and those which cause the most radiative forcing. To avoid the observational biases in the population of contrails, a modelled inventory of contrails is used.

The CoCiP-derived contrail dataset of Teoh et al. (2023) provides a global inventory of contrail segments globally at 5 minute intervals, derived from air traffic data. These segments are the result of the application of CoCiP for flights in 2019–

170 2021, produced using the pycontrails implementation of the model in Python (Shapiro et al., 2023), including radiative forcing estimates based on the parameterisation of Schumann et al. (2012). Air traffic is based on the GAIA emissions inventory (Teoh et al., 2023), which showed good agreement with other flight inventories, and showed only a small deficit compared to major airport statistics. This population of contrails should not be expected to match observations on a flight-by-flight basis. It is produced using the ERA5 meteorological reananlysis, which has difficulty producing accurate ice-supersaturation fields at

175 flight altitudes (Gierens et al., 2020). However, it is expected that the statistics of this population are aligned with the population of actual contrails. This database is suitable for this study because contrail observability is to be tested independently of the

specific meteorological context. The following analysis is based only on the distribution of contrail properties which drive observability to first-order.

Two populations are used for different parts of this work:

180   1. The 'instantanous' sample, constructed from global contrail datasets at 114 timesteps randomly-sampled through 2019, with minimum separations of 24 h. This is approximately 14 million contrail waypoints in total. The timestamps are well-distributed seasonally and throughout the day, so are representative of seasonality and the diurnal cycles of warming and air traffic.

    2. The time-resolved dataset, wherein the properties of all contrail segments that formed in a 24 h period between 1200
185   UTC on 2024-01-06 and 2024-01-07 were tracked for their whole lifetime, up to 12 h after their formation (at which time they would be removed by CoCiP). Around 1 million contrail segments are formed in the 24 h window, forming a dataset of 34 million segments as they evolve.

The contrail data is analysed as a set of contrail segments—partial lengths of contrail which form over 5 min intervals. This supports the analysis of geometrically extended contrails with varying meteorological conditions and properties along
190   their length. Each contrail segment persists in the CoCiP model until one of a range of end-of-life conditions is met, including optical depth, ice crystal number concentration, and altitude thresholds or if their age exceeds 12 h, detailed in Teoh et al. (2023). The length of time for which a contrail segment remains in the model is termed the 'persistence lifetime' for this work.

Some variability in the properties of the contrail population is caused by seasonal and diurnal variations in both meteorology and air traffic. The extent that this variability leads to changing contrail observability is tested by subsetting the instantanous
195   sample (population 1) by month and 'daytime' contrails (0600–1800 local solar time) and 'nighttime' contrails (1800–0600 local solar time). Using globally-consistent thresholds, rather than local solar time, highlights variability in the instantaneous contrail population globally rather than the local conditions. The standard deviation in observability fractions derived on each of these subsets is used as an uncertainty caused by seasonal and dirunal variability.

CoCiP is not a perfect model, and some flaws in the distribution of contrails are clear in the red histograms of properties
200   from the CoCiP population shown in Fig. 3. These include a high frequency of contrails at the maximum depth in Fig. 3(e) (1.5 km) and the occasional occurrence of very wide contrails in Fig. 3(c) for which assumptions of linearity and homogeneity across the width are likely to break down. Nonetheless, the model has found broad-based application (Jeßberger et al., 2013; Schumann et al., 2015; Voigt et al., 2017; Teoh et al., 2020, 2023), and the population of contrails produced has been shown to align with in-situ and satellite observations (Schumann et al., 2017; Voigt et al., 2017).

205 **3 Contrail parameter observability tests**

3.1 Single parameter sensitivity tests

Contrail IWP, r_{eff}, width, altitude and width were each varied while holding other properties constant. The impact on the detected w_{eff} (equation 4) of these parameters is shown in Fig. 3, with the mean effective width across four realisations, $\overline{w_{\mathrm{eff}}}$,
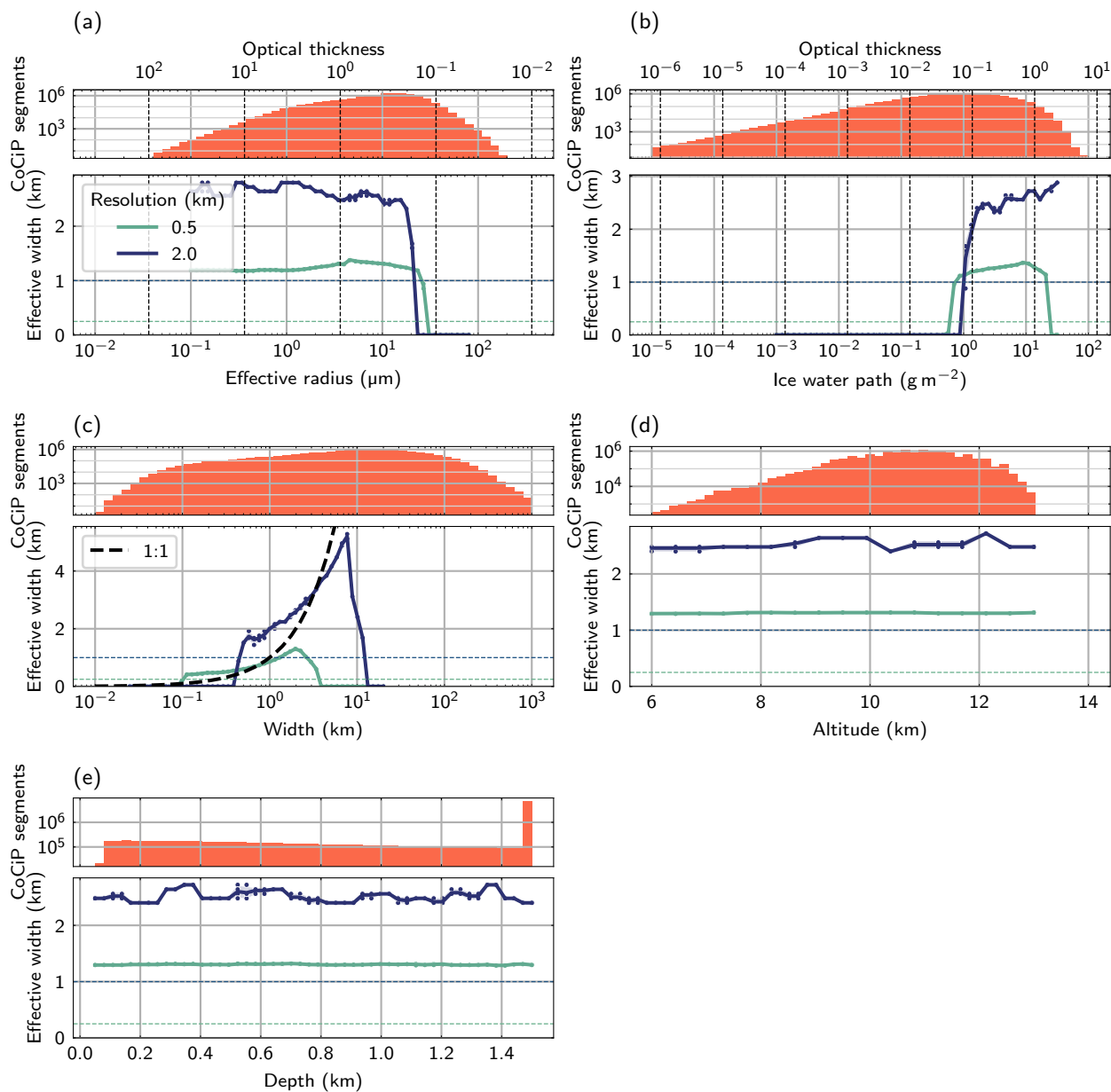
Figure 3. Tests for changes in contrail observability (i.e. observed effective width) when varying r_{eff} (a), IWP (b), width (c), altitude (d) and depth (e) of contrails. Blue-green solid lines are detected $\overline{w_{\mathrm{eff}}}$ averaged over 4 noise realisations for two different imager resolutions, the corresponding dashed lines are the $w_{\mathrm{eff}} \geq R/2$ condition for detection. The response is plotted alongside histograms of the CoCiP model population's properties. Based on the instantaneous contrail sample. A black dashed line in panel (c) indicates equal w_{eff} and prescribed contrail width.

shown with the solid line, and individual w_{eff} measurements shown as scatter points. $w_{\text{eff}} = R/2$ thresholds for detection are
210   shown as dashed lines.

In each observability test, properties are varied with respect to a baseline contrail, which is 2 km wide, 0.5 km deep, has a base
altitude at 11 km, r_{eff} of 10 µm, and IWP of 2 g m^{-2}. The baseline properties are chosen as representative of the instantaneous
contrail sample of Section 2.3 (population 1), histograms of which are shown alongside the observability response. The r_{eff},
IWP and width of this baseline contrail are marked with a blue cross in histograms of this population Fig. 5(b,c).

215   There is a low-optical-depth observability limit seen in the high-r_{eff} and low-IWC regimes of Fig. 3(a,b)—as expected,
contrails which are too optically thin are unobservable. Very optically thick contrails also appear undetectable, creating a high-
IWP limit of observability seen for the 0.5 km resolution imager in Fig. 3(b). This high-IWP limit occurs when the centre of a
contrail becomes so optically thick as to appear opaque to the upwelling thermal radiation in both imager channels which are
differenced for the brightness temperature difference signal (used for contrail detection, Section 2.2).

220   A significant observability response occurs as contrail width is increased, shown in Fig. 3(c). The narrowest contrails are
not detected, with an observability onset occuring as contrail width increases to (slightly below) the imager resolution. $\overline{w_{\text{eff}}}$
then increases from an initial approximately one-pixel effective width, detecting the broadening contrail. Note that a directly
comparable contrail width is not straightforwardly produced using imagers with different spatial resolutions. The same under-
lying contrail produces contrails of different pixel mask areas, so different $\overline{w_{\text{eff}}}$ and inferred width. This is analogous to the
225   dependence of cloud fraction on the resolution of a binary cloud mask, found by Shenk and Salomonson (1972).

Wide contrails are also not detected. This is a limitation of the detection algorithm used—which uses line kernels that
highlight linearly-extended regional gradients 1–4 pixels wide. The CoCiP population has a significant spread in width, in-
cluding contrails with widths of up to several hundred kilometres, so this algorithm limitation would have a significant effect
if untreated. These wide unobservable contrails are likely to be detectable if a different approach is used, given that narrower
230   contrails with similar microphysics have been identified using this algorithm. To assess the impact of a less conservative con-
trail detection algorithm, detectability thresholds are adjusted to only include low-width unobservability behaviour, detailed in
Section 3.2 (the adjusted threshold in Fig. 5).

The contrail altitude is expected to limit the brightness temperature contrast between the contrail and clear-sky regions of
an image, limiting observability. However, contrail altitude is not found to have a significant effect on the observability of this
235   particular baseline contrail (Fig. 3(d)). This becomes important when contrail width is less than the imager resolution, as shown
in Fig. 4, where detectability has been tested at a range of altitudes for contrails with sub-grid widths over ten noise realisations.
The detection probability is shown to co-vary with altitude and width, for contrails with width significantly below the imager's
resolution (of 2 km). Higher contrails have greater brightness temperature contrast than lower contrails, so become observable
at narrower widths (as discussed in Section 2.1 and Mannstein et al., 1999), however this effect is small for the altitudes at
240   which contrails form.

The vertical depth over which the contrail's IWP is spread also does not drive a strong observability response (Fig. 3(e)).
This relaxes any observability bias that may emerge from the unrealistic distribution of contrail depths in the CoCiP histogram
of Fig 3(e).
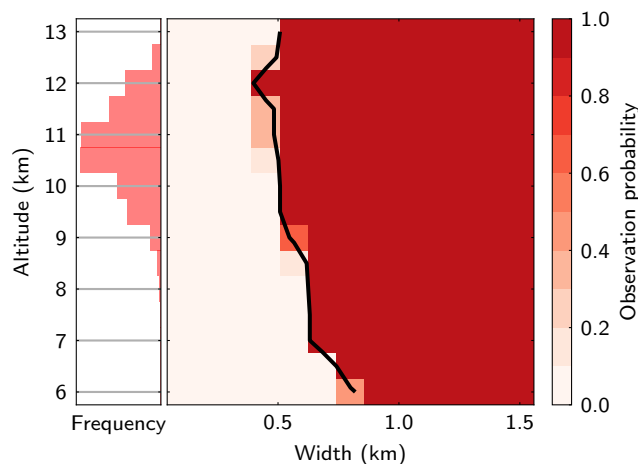
Figure 4. The observability of contrails as width with respect to the baseline contrail. Tested for a simulated 2 km resolution imager. The black contour shows the observability threshold.

3.2 Contrail observability threshold

245 IWP, r_{eff}, and contrail width have a strong control on contrail observability (Fig. 3). This aligns with expectations: contrail observability ought to depend on the contrail optical thickness (to first order, a combination of r_{eff} and IWP), and the interaction of the contrail's geometry with the imager's pixel resolution. A sensitivity to altitude was also observed for narrow contrails (Fig. 4), although dependence on altitude is weak at the higher altitudes where most contrails exist. An altitude of 11 km has been assumed for all contrails—this is approximately consistent with the modal altitude (Fig. 3(d)), and aligns with the aim of a

250 maximally-observable case (Fig. 4). The observability of a contrail was tested in the identified parameter space: covarying IWP, r_{eff}, and width. Histograms in this space at constant width are shown in Fig. 5, alongside a derived observability threshold. The population has been split into logarithmically-spaced bins in each dimension—including contrail width bins between 0.025 and 25 km wide. Slices of these histograms at contrail widths narrower than, comparable to, and wider than imager resolution have been shown—illustrative of different observability behaviours. The logarithmic scale is most appropriate for resolving

255 the width distribution and observability threshold (as in Fig. 3(c)).

Fig 5(a, b, and c) are observability test results for contrails approximately 2 km wide, in images using a simulated 2 km resolution imager. In Fig. 5(a), the detection probability is shown as a function of the parameter space. Contrails with a larger optical thickness tend to be more observable than those with a lower optical thickness. The observability threshold, $P_{\mathrm{obs}} > 0.5$, is shown as a black contour. Fig. 5(b) shows the observablity threshold with the distribution of contrail segments

260 with approximately this width, taken from the instantaneous contrail sample. Fig. 5(c) is as Fig. 5(b), with the population weighted by the net radiative forcing. For these 2 km contrails, the observability threshold splits the population (Fig. 5(b)), but the segments generating strong radiative forcings are generally observable (Fig. 5(c)).
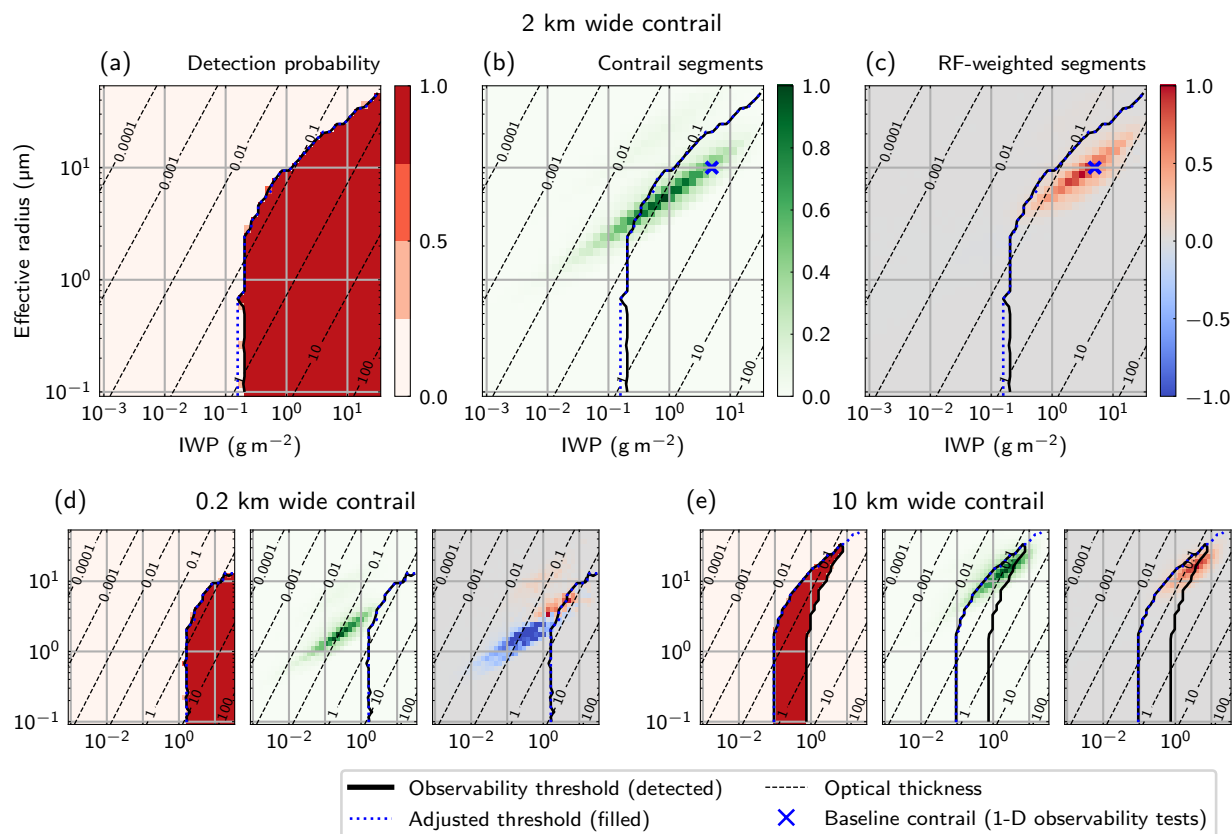
Figure 5. Illustrative slices from a 3-D contrail observability test, including: observability quantified using effective width (a), and histograms of CoCiP populations weighted by occurrence (b), and net radiative forcing (c), for 2 km wide contrail segments. Similar histograms are shown for 0.2 km wide contrails (d) and 15 km wide contrails (e). The 'adjusted threshold' represents the observability threshold adapted to include all theoretically observable contrails, without the high-width algorithm deficiency.

For contrails significantly narrower than the imager's resolution, a higher contrail optical thickness is required to detect the contrail (Fig. 5(d), compared to (a, e)). It is notable that sub-pixel-width contrails can still be observable, but that any single 'optical thickness threshold' is insufficient for characterising contrail observability. Observability also depends on both the contrail microphysical and geometrical properties, especially the contrail width relative to the imager resolution.

When tested against contrails wider than the imager's resolution (shown for 10 km wide contrails in Figure 5(e)), contrails are markedly less detectable, corresponding to the high width unobservability observed in Section 3.1 (Fig. 3(c)). Optically-thick wide contrails are preferentially undetected compared to more optically thin ones at the same width—this is because the more optically thin contrails can be detected as a narrower contrail by detection of only the central part where the IWP peaks. As discussed in Section 3.1, this high-width undetectability is a property of the detection algorithm used. The observability
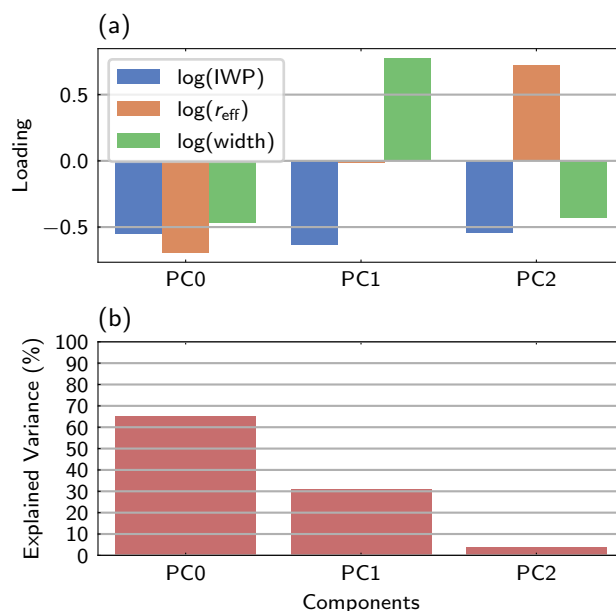
Figure 6. The principal components (PCs) of the CoCiP population in an IWP–r_{eff}–width parameter space. (a) shows the PC loadings with each variable, and (b) shows the percentage of variance explained by variability in the direction of this PC.

threshold is adjusted to treat all contrails wider than the narrowest detected contrail with the same IWP and r_{eff} as detectable. This adjustment is shown using the dotted blue contour in Fig. 5.

The 'cause of unobservability' for an unobservable contrail with a given set of properties is also defined in terms of the
275   adjusted 'theoretically observable' (blue dotted) threshold derived here. Any contrails for which there exists a wider, theoretically observable contrail with the same IWP and r_{eff} (therefore, the same peak optical thickness) are deemed 'too narrow', other unobservable contrails are 'too optically thin'.

3.3   Principal components of variability in the parameter space

Through the 1-D analyses of Fig. 3, it is clear that the observability is a strong function of the three parameters used for
280   the observability space (IWP, r_{eff}, and width). The histograms of Fig. 5(b, c, d, and e) suggest that the CoCiP population approximates a plane in this space (on logarithmic axes). This behaviour is important to enable robust application of the derived observability threshold.

Principal component (PC) analysis (Lever et al., 2017) can indicate the key directions of variability, and the amount of population variability which exists in these emergent directions. Examining the PCs and their associated proportion of variance
285   enables us to establish to what extent the population lies on on a plane in this space, and the principal components offer some physical insight. Values of $\log(\mathrm{IWP})$, $\log(r_{\mathrm{eff}})$, and $\log(\mathrm{width})$ are standardised to have unit variance before analysing because of their different scales.
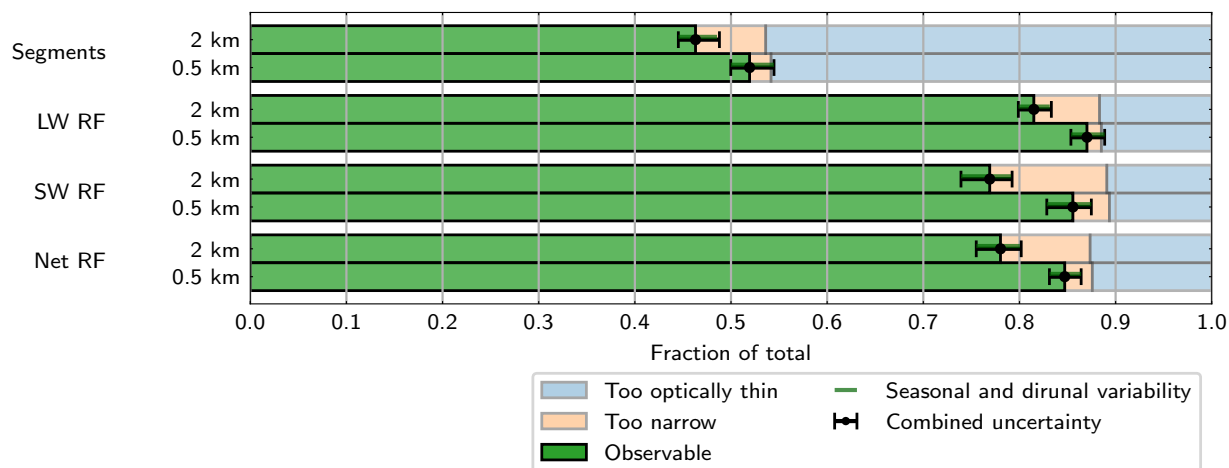
Figure 7. The theoretically observable fraction of contrail segments and instantaneous SW, LW, and absolute net radiative forcing, based on the CoCiP populations using Jet-A1 fuel. Error bars are a combination of the variability due to seasonal and diurnal effects (also shown independently), and uncertainty in the derived threshold based on the observable proportion using 0.25 and 0.75 P_{obs} thresholds.

Fig. 6(a) shows the principal components within this parameter space, and Fig. 6(b) shows the associated proportion of the variance. Together, PC0 and PC1 describe 96 % of the variance of the population. PC0 is a component describing IWP, r_{eff} and width covarying—i.e. bigger contrails tend to be more optically thick, presumed to be related to the temporal growth of the contrail. PC1 comprises anti-correlated IWP and width, at approximately constant effective radius—this can be interpreted as contrail segments at a different point in their evolution, with the fixed population of ice crystals being spread over a growing width as a segment ages. The correspondence of these principal components to the time-evolving properties of the model population are illustrated in the below analysis of population 2 (Fig. 8).

4   Population observability consequences

4.1   Contrail segment observability

Fig. 7 shows the percentage of contrail segments which are observable using simulated 0.5 km and 2 km resolution imagers. The observable fractions are based on the combination of the instantaneous contrail sample described in Section 2.3 (population 1) and the observability threshold found in Section 3.2, including the wide-contrail correction. (46 ± 2) % of contrail segments are observable in 2 km resolution satellite images, this increases only 7 percentage-points when a 0.5 km imager is used. Examining the causes of unobservability, the observability gain is minimal because the significant majority of unobservable contrails are too optically thin to be observed, rather than too narrow. Optically thin contrails are not as accessible via imager

resolution enhancements—observations of these cases are instead limited by detection algorithm thresholds, and ultimately imager noise.

305 (78 ± 3) % of absolute net contrail forcing is theoretically observable in simulated 2 km resolution images (Fig. 7). This means that the contrails with stronger radiative forcing are a more observable population than the wider contrail population. This aligns with expectation: a small percentage of strongly-forcing contrails contribute most of the net warming (Teoh et al., 2022a), and more optically thick contrails tend to warm strongly (Meerkötter et al., 1999).

Contrails that have a strong LW forcing are typically more observable than those with a strong SW forcing. This is be-
310 cause the cooling (SW-forcing) population tends to consist of narrower (younger) contrails. This is visible by comparing the SW-dominant and LW-dominant regions of the net forcing CoCiP population in Fig. 5. This may be caused in part by the combination of the daytime-only nature of SW forcing and the daytime bias of air traffic (Schumann and Heymsfield, 2017). As a result, the discrepancy between LW and SW components is less in the higher-resolution imager.

The uncertainties given are a combination of the P_{obs}-derived threshold uncertainty (described in Section 2.2) and the sea-
315 sonal and dirunal variability (described in Section 2.3). The component due to seasonal and diurnal variability is also shown independently on Fig. 7. The combined uncertainty is dominated by the seasonal and dirunal component, indicating that the observability threshold is well-defined with respect to different realisations of the noise field.

The contrail observability is dependent on the contrail detection algorithm used. The observability threshold (derived in Section 3.2) is based on the lowest width for which a set of of optical-thickness-driving microphysical properties (i.e. r_{eff} and
320 IWP) produces simulated brightness temperature field in which the contrail is detected using the Mannstein et al. (1999)-like detection algorithm introduced in Section 2.2. The algorithm used contains thresholds as distributed with McCloskey et al. (2021), tuned on human-labelled datasets to maximise precision and recall—making these results reflect the contrails which would be observable as distinct objects by human labellers. A less-conservative detection algorithm was tested, based on reducing the threshold from the human-labelled tuned value to the least-conservative between this and the value identified by
325 Mannstein et al. (1999). The threshold derived using this adjustment is shown with with an evolving contrail in Fig. 8 (b). In this case—using the same high-width adjustment of Section 3.2—(89 ± 1) % of segments and more than 95 % of all components of forcing is theoretically observable in fields simulated with 2 km resolution. This suggests that the observability limit derived here can be relaxed if false positives can be avoided, for example in the case of targeted observation of specific contrails based on advected flight tracks, where a likely location of the contrail is known.

330 To illustrate the significant impact caused by background cloud—and demonstrate that this is a maximum accessible fraction of contrails, the observability of contrails has been tested against a layer of background cirrus. The cirrus layer significantly reduces the brightness temperature contrast between the contrail and the background, decreasing contrail detectability. Detectability has been tested using the same thresholds based on human-labelled datasets described in Section 2.2. Under this analysis, fewer than 2 % of contrail segments in the instantaneous sample were detectable, and less than 5 % of each com-
335 ponent of forcing is theoretically observable. The derived minimum-width threshold for observability is illustrated in Fig. 8(c). Only significantly more optically-thick contrails were detectable. A high-IWP limit of detectability seen in this observability threshold (as in of Section 3.1, Fig. 3(b))The minimum width required for detection shows a discontinuity at high-IWP. In this case the combination of
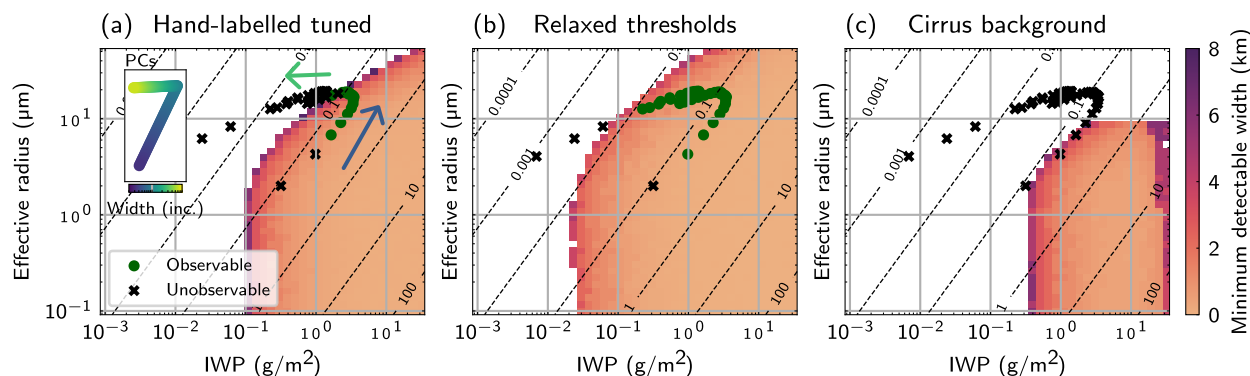
Figure 8. Representative trajectories of a contrail's evolution in parameter space. The contrail IWP and r_{eff} at each model timestep is marked against the minimum detectable width for a given observability test using detection algorithm thresholds: tuned to hand-labelled data—as distributed with McCloskey et al. (2021) (a), with the thresholds reduced to the least-conservative values between the Mannstein et al. (1999) and McCloskey et al. (2021) implementations (unachievable for passive detection in real data) (b), and against a layer of background cirrus (c). The same detection algorithm is used for panels (a) and (c). Also included (on inset axes to panel (a)) are the principal components identified in Section 3.3, coloured by their evolving width, which broadly correspond to the stages of contrail evolution (arrows).

background cirrus and contrail causes does not cause a brightness temperature difference signal at the centre of the contrail as it is sufficiently optically thick to be opaque in both the channels that are differenced. Wider contrails with similar optical

340   thickness are detected, because less-optically-thick parts of the contrail exist which remain detectable.

4.2   Observability with contrail aging

A contrail's properties evolve as it ages, so observability also has characteristic evolution. The evolution of one contrail from the time-evolving sample (population 2) is shown against the different observability thresholds derived is shown in Fig. 8. This behaviour is typical of the time-evolving dataset. The stages of evolution (growth, persistence, and dissipation) broadly

345   align with the two PCs identified to explain a large proportion of the variance (Section 3.3). The observability status of the contrail is marked—examining Fig. 8(a), at formation it is initially too narrow to be observed, but as it grows the minimum observable width threshold is crossed, and the contrail becomes observable. During the persistence phase, the contrail spreads over a wider area, decreasing the IWP of the contrail at approximately constant effective radius. During this time this contrail becomes unobservable, due to being too optically thin. Finally, this contrail dissipates, with ice crystals eventually decreasing

350   in size, until it is removed from the model population at its 'end of life'. Fig. 8(b,c) repeat the parameter-space trajectory and observability status using a less-conservative algorithm and when observed against a layer of background cirrus respectively (the thresholds as described in Section 4.1).

Fig. 9 shows the proportion contrails which are observable as they age in the time-evolving sample (population 2) along with the proportion of LW forcing. Each contrail segment has been tracked for its entire CoCiP lifecycle (which was capped at

355   12 h), and observability has been assessed at each timestep. Data is binned based on model timesteps since formation, that is,
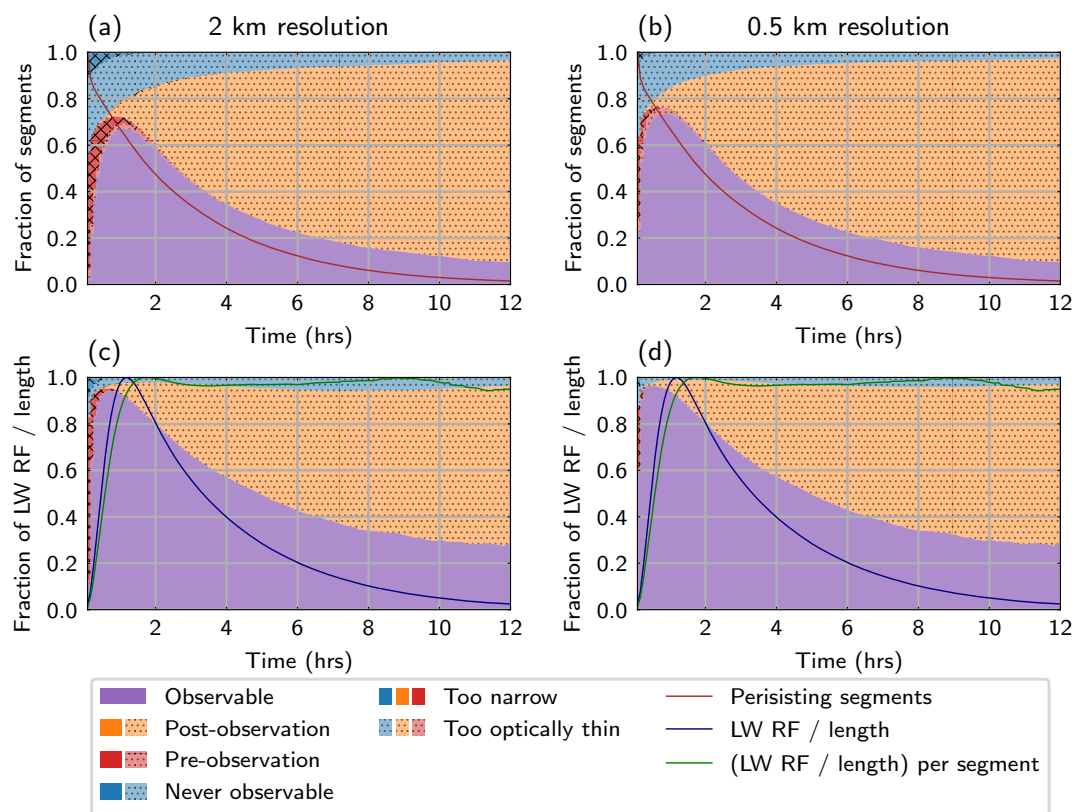
Figure 9. The time evolution of observability—the observability status of contrail segments formed globally within the time-evolving sample, using Jet-A1 fuel.

contrails in the first bin were formed between 0 and 5 minutes ago and have survived until the time at which the model outputs data. This means that some contrails with persistence lifetime less than 5 minutes are never represented in the analysis, similar to the population of contrails captured in regular satellite observations.

Using the adjusted observability threshold of Section 3.2 (Fig. 5; Fig. 8(a)), contrail segments have been categorised as either
360   theoretically observable (purple), or unobservable (red, orange, and blue). Unobservable contrails are either never observed with this imager before their dissipation (blue), have not yet been theoretically observable but will be observable later in their lifecycle (red), or have been previously observable but are no longer (orange). Unobservable contrails have again been categorised as either too narrow (full coloured and hashed) or too optically thin to be observed (muted colours and dotted).
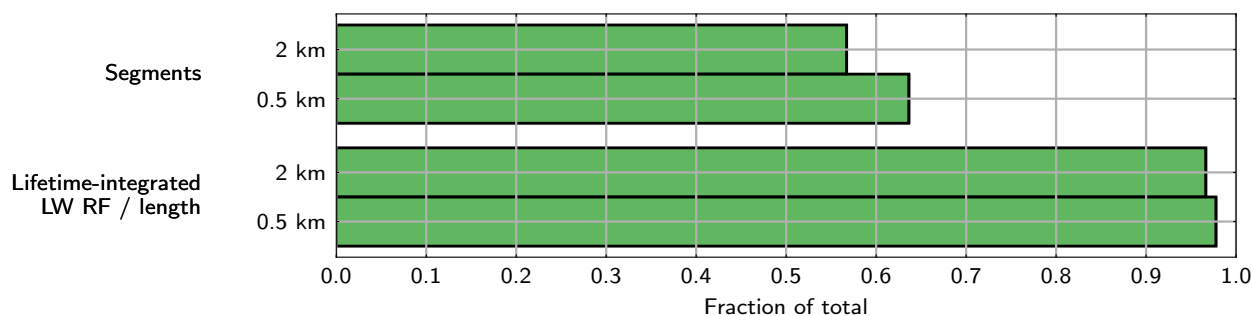
Figure 10. The proportion of time-evolving contrails observable for at least one model timestep, as determined using contrail detection algorithm threshold tuned on hand-labelled data (the algorithm as distributed with McCloskey et al. (2021)).

A small number of contrail segments are temporarily unobservable after their period of observation; these are classified as
365 'post-observable' while unobservable—this affects 8 % of segments in the 2 km imager and 7 % in the 0.5 km imager.

Each of the panels are overplotted with relevant integrated quantities. The surviving proportion of segments is shown in Fig. 9(a,b) and the instantaneous LW forcing per unit length (both integrated over the surviving contrails and per contrail) is shown on Fig. 9. Note that the per-segment forcing per unit length peaks at just less than two hours after formation, remaining at this value for the remainder of the persistence, although the total decays as some contrails dissipate (Fig. 9(c, d)).

370 The population of never-observable contrails (blue) consists of both narrow and optically thin contrails. This population is much reduced in the forcing-weighted analyses (Fig. 9(c,d)), suggesting that keeping track of these contrails is less important for monitoring the radiative forcing. For trials attempting to mitigate the formation of contrails, it is important that these contrails are avoided as they would lead to false negatives—inference of no contrail when one has actually formed.

Pre-observable contrails tend to be too narrow to be observed, becoming observable when they have broadened sufficiently.
375 A pre-observable population persists into the forcing-weighted case, so these contrails also play an important radiative role. The high-resolution imager provides a significant improvement in accessing this population.

When the contrails are no longer observable, they are overwhelmingly more likely to be too optically thin than too narrow. It is at this stage that contrail observability appears to decouple from the contrail lifetime—the post-observable phase doesn't seem to be a transient phase as the contrail dissipates, but a growing proportion of the contrails. Again, it should be noted
380 that the number of contrails and total amount of forcing are increasingly small with aging, so this increasing fraction remains relatively small as a fraction of the instantaneous population.

As a check for consistency with the analysis of Fig. 7, the proportion of observable contrails has been integrated with the corresponding total. Approximately 45 % of contrail segments are found to be theoretically observable with the 2 km imager, increased to 50 % for the 0.5 km resolution imager; 69 % and 70 % of LW forcing is theoretically observable for the 2 km
385 and 0.5 km resolutions respectively. These are slightly smaller than the the values based on the instantaneous sample, Fig. 7. Comparing to the variability ranges derived based on population 1 (Fig. 7), the portion of observable segments lies within
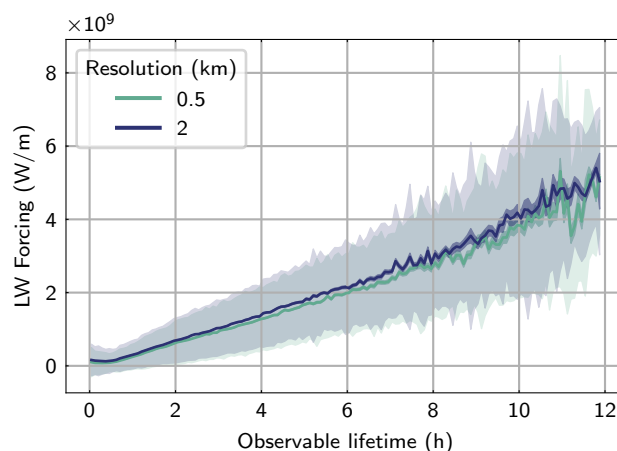
Figure 11. The relationship between lifetime-integrated forcing per unit length, and the observable lifetime. The bold region denotes uncertainty in the mean, and the lightly-shaded region is the variability.

variability, and the observable fraction of LW forcing does not. This highlights that daily variability in contrail properties and estimated forcing is even more extreme than seasonal variability.

The number of population 2 contrails observed at least at some point during their lifecycle was also found is plotted for both the model population of segments and the lifetime-integrated LW forcing per unit length in Fig. 10. Around 57 % of contrail segments are observable in 2 km resolution images for at least one model timestep during their evolution. This increases to 64 % with the 0.5 km resolution imager. When weighted by their lifetime-integrated LW forcing, this is increased to 97 % and 98 % for the 2 km and 0.5 km resolution fields respectively. Uncertainty in these values is expected to be dominated by seasonal and diurnal uncertainty (as in Fig. 7), and has not been calculated for the time-evolving sample (population 2).

Finally, the distribution of the times at which a contrail first becomes observable are examined. This transition is highly skewed, so the median age of first observability is given, with the first and third quartiles are given as an uncertainty range. In 2 km resolution images, detection first occurs at (21^{+73}_{-11}) min, whereas observation occurs at an age of (9^{+61}_{-4}) min in hypothetical 0.5 km images. This is in good agreement with the delays to onset of GOES (ca. 2 km resolution) observation reported by Chevallier et al. (2023); Gryspeerdt et al. (2024).

4.3 Observable lifetime as a proxy for radiative importance

Radiative forcing during the part of the lifetime for which a contrail is unobservable may be significant. A fraction of contrails has been found both before and after their period of observability, including when weighted by their forcing (Fig. 9). Radiative importance conclusions drawn from observed contrail lifetime therefore carry an implicit assumption that the factors influencing the period of observability also determine the persistence lifetime of the contrail. This assumption is threatened by the 'too optically thin' post-observable fraction found here. Previous contrail tracking studies have inferred contrail lifetime from observed lifetime, requiring assumptions about initial contrail spreading rates and the generalisation of observation-derived sur-
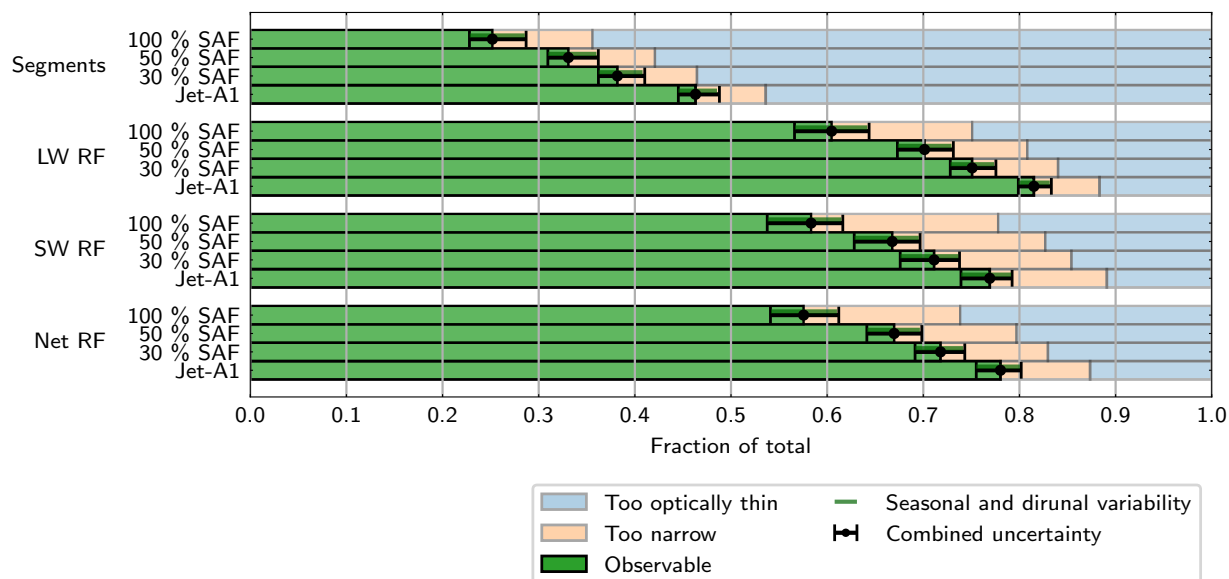
Figure 12. The theoretically observable fraction of contrail segments and instantaneous radiative forcing, based on the CoCiP populations assuming a fractional adoption of SAF biofuel. Observability has been tested for a simulated 2 km imager for contrails in an otherwise clear sky. Error bars indicate the observable proportion using 0.25 and 0.75 P_{obs} thresholds.

vival functions to unobserved parts of a contrails lifetime (Gierens and Vázquez-Navarro, 2018). The length of time for which a contrail appears in consecutive geostationary satellite images—the 'observable lifetime' of the contrail—is measurable. We now examine the relationship between this observable lifetime and its lifetime radiative impact.

410   Fig. 11 shows the lifetime-integrated LW energy forcing per unit contrail length as a function of the theoretically observable lifetime for the contrails in the time-evolving sample. For both current imagers and theoretical higher-resolution imagers there is a positive correlation, with an approximately linear relationship between the observable lifetime and the LW radiative forcing for contrails observable for longer than 1 h.

There is significant variability in each observable lifetime bin, but a resolution dependence is well-resolved. Observed

415   contrails tend to have higher lifetime forcing in more coarsely-resolved images. This follows from the ability of the 2 km resolution imager to only observe larger and more optically thick contrails, which in turn have stronger forcing.

4.4 Observability with the adoption of alternative fuels

Fig. 12 shows the potential observability consequences of decreased emission of activating particulates—dominated by soot while current fuels. The observability of a contrail population formed during fractional adoption of alternative fuels has been

420   determined. The population results from CoCiP, run with identical flights and meteorology, but assuming a fractional adoption of SAF in the fuel in all aircraft (rather than Jet-A1 fuel) results in decreased ice emission indices. The modelling methodology

follows that of the SAF experiments of Teoh et al. (2022b)—using the 30 %, 50 %, and 100 % SAF adoption experiments, which have been expanded to the global flight inventory of Teoh et al. (2023).

There is a significant decrease in the observable fraction of contrail segments and forcing. In less a soot-rich environment,
425   fewer contrail ice crystals form, so they grow larger (Voigt et al., 2021). A shift in the populations of Fig. 5 towards higher effective radius (and lower optical thickness) moves the contrails nearer the observability threshold, corresponding to these drops in observability. In simulated 2 km images after 100 % adoption, only (25 ± 3) % of segments are observable, and only (58 ± 4) % of net forcing is theoretically observable. Uncertainty is again dominated by seasonal and dirunal variability (as Fig. 7). This means that coverage estimates for contrails produced by aircraft generating fewer non-volatile particulates will be
430   based on fewer observations, making them (and potential assessments of radiative impact) more uncertain.

Teoh et al. (2022b) explores the derived climate benefit of SAF adoption. It should be noted that, while a lower fraction of contrails is observable, there are also fewer contrail segments in the CoCiP population, and a reduced net contrail forcing. The activation of volatile particulates in less soot-rich exhaust (Ponsonby et al., 2024) has not been considered for this model population. Volatile activation would act to partially counteract the changes in observability driving the decreased observable
435   fraction found here.

5   Discussion

5.1   Applicability of methodology

This analysis is limited to the very simple case of a straight-line contrails against a plain ocean background, with obstacles to observation from imager properties, and the thresholds from the algorithm applied. The algorithm, trained on hand-labelled
440   contrails, provides insight into the contrails practically accessible in real satellite images (beyond the absolute limits of detection in the artificial radiance fields, imposed only by imager resolution and noise).

The minimally-realistic synthetic contrails modelled here are intended as maximally-detectable test case. This approach is designed to establish whether some contrails go undetected with current instruments even in the most straightforward case. The approach also treats contrails as extended objects—testing not only that contrails produce a signal but that the extended signal
445   is detectable as a contrail, aligning with detection methods that take the spatial properties of the contrail into account. The brightness temperature contrast, and particularly background inhomogeneity, has been noted to be important for the detection efficiency (Mannstein et al., 1999). Contrails imaged over land or against background cloud should be expected to be less observable than is established using this analysis because this will introduce additional features with reduced contrast to the brightness temperature fields used for detection, owing to their colder temperatures (particularly for underlying cloud) or
450   reduced emissivity (particularly for surface features). Additional factors influencing contrail observability are likely to include contrail latitude, and satellite zenith angle more generally, which would affect the dimensions of the imaged grid, and optical paths for radiative transfer (Maddux et al., 2010). These variations within regions of the same satellite field of view have not been considered, to simplify the parameter space and the analysis of unobservability causes. This also aligns the approach with the best-case observability. The analysis in this work is restricted also to a single atmospheric profile (the US standard

455 atmosphere). More-physical atmospheric profiles would also impact brightness temperature contrast slightly, but this smaller effect has not been treated here, again decreasing complexity and allowing more-direct consideration of the cause of detection limits. Additionally, the use of 1-D radiative transfer simulations neglects 3-D effects (Cornet et al., 2010).

Uncertainty in the derived threshold relative to instrument noise has been found to be small relative to seasonal and diurnal variations in the instantaneous population of contrails and their estimated radiative forcing. This highlights the importance of 460 considering changes to contrail observability in specific observational contexts. The variability in observability has been found as a result of the changing contrail properties alone—not the varying meterology. It is clear that meterology will play a further role, based on the adjusted threshold of Fig. 8(c) in the presence of background cirrus. Unconsidered uncertainties include the CoCiP-derived population and contrail properties.

5.2 Relevance to applications of contrail observation

465 The fact that some contrails remain unobservable in these tests demonstrates that these results are relevant considerations for observational applications, such as the observation of contrail radiative forcing. Fig. 7 indicates that (22 ± 2) % of net contrail forcing goes unobserved in current 2 km resolution geostationary imagers, and Fig. 5 shows that there is a microphysics dependence beyond a simple optical thickness threshold for observability. This is due to a combination of contrails whose observation is optical-thickness and resolution limited, of which, only the too-narrow contrails are accessible in theoretical 470 higher-resolution images. As seen in Fig. 9(d) as compared to Fig. 9(c), this corresponds to the observation of contrails earlier in their evolution should resolution be improved. Particular care is needed to compare contrail coverage when there is a change to contrail microphysics—such as in the adoption of biofuels, Fig. 11—where a change in observability may have been induced. Further caution is needed when comparing masked contrail grids on images with different resolution—in Fig. 3, different effective width values are measured when using different imagers.

475 One may seek to determine the efficacy with which contrail formation has been mitigated, for example, in a trial attempting to avoid forming contrails (Molloy et al., 2022). For this, effective flight matching is required as well as efficient detection, as described in Geraedts et al. (2023). It has been shown that the majority of instantaneous forcing is theoretically observable using current instruments (Fig. 5) when tested in the ideal case shown here. Futhermore, in Section 4.2, 97 % of lifetime-forcing weighted contrail segments are shown to observable at least for some time in their evolution. This provides reassurance that 480 most of the most climate-relevant contrails are observable at some time during their lifecycle. Effective flight matching relies on the detection of contrails shortly after their formation—to minimise any errors that develop between advected flight path and detected contrail. Here a higher-resolution contrail detection technique makes a significant difference—most contrails are detectable within 9 min of their formation (Section 4.2), compared to 21 min for the 2 km imager.

A final application in need of improved contrail observation is the validation of contrail models, a need laid out by Schumann 485 et al. (2017) and Kärcher (2018). The thresholds derived here form a foundation to consider which contrails are observable and how many may need to be observed to draw confident conclusions about the predictive power of the models. These validation tasks often then require retrieval of the contrail cirrus properties and variability beyond just the simple detection of contrail

coverage. Care is required in applying instruments to this task, illustrated by the varying effective widths measured for the same contrail imaged at different resolutions, Figs. 2 and 3.

6   Conclusions

Infrared imagers carried by geostationary satelllites are well-placed to make widespread observations of the time-evolving properties of contrails. The detection of contrails is limited both early and late in their evolution: imaged radiance fields are coarsely resolved with respect to the geometry of young contrails, and aged contrails are wide and disperse. This work highlights the contrails that should not be expected to appear in images from geostationary satellites, even in the most ideal conditions, as a function of contrail properties and detection methods.

Satellite contrail observation has been simulated for simple straight-line contrails with a Gaussian profile, against a plain background, laid out in Fig. 1. A Mannstein et al. (1999) style line filtering algorithm has been used to test the observability of contrails in these simulated radiance fields (Fig. 2) modelled with different properties. First, contrail width, IWP, r_{eff}, depth, and altitude were varied independently (Fig. 3). Altitude was not seen to be a major driver of unobservability, particularly at altitudes where contrails exist (Fig. 4). Then, an 'observability threshold' is found by covarying the properties which produced strong observability responses (IWP, r_{eff}, and contrail width). The threshold is shown relative to distributions of the properties of a model-derived population of contrails (Population 1 of Section 2.3) at three different constant widths (and their forcing) in Fig. 5.

The observability threshold was applied to this modelled population of global contrails—determining the observability of the instantanous population based on a sample distributed in time of day and year (Fig. 7). The most radiatively important contrails are more likely to be theoretically observable than the population as a whole. The unobservable fraction of the instantaneous global population of contrails varies from (54 ± 2) % (of contrail segments in 2 km resolution images) to only (13 ± 2) % (of LW forcing in 0.5 km images), shown in Fig. 7. The observability is strongly sensitive to the the background—a simple layer of background cirrus shifts the observability threshold to include only the most optically thick contrails (Fig. 8(c)), obscuring detection of almost all contrails in the population.

The threshold was also applied to the time-evolving properties of contrails (Fig. 8). By analysing contrail segments forming globally over a 24 h period (Population 2 of Section 2.3) the evolving observability behaviour (Fig. 9) was derived. Most contrails are theoretically observable at least at some point in their evolution. Around 57 % are visible in current 2 km resolution imagers, comprising 97 % of the total radiative forcing from the contrail population (Fig. 10).

It has been shown that the average lifetime radiative forcing is a strong function of the observable lifetime for the contrail population forecast by CoCiP (Fig. 11). This relationship enables radiative-importance conclusions drawn from the length of time for which a contrail is observed. Factors not considered here may obscure this result, particularly the development of a contrail outbreak or other meteorological evolution.

Finally, these satellite observations' limitations are important when assessing the efficacy of climate change mitigation strategies. It has been shown that widespread adoption of cleaner-burning fuels would lead to a significant drop in contrail

observability, with a 20 percentage-point drop in the observable fraction of net instantanous contrail radiative forcing under a modelled decrease in ice crystal number with the theoretical complete adoption of SAF (Fig. 12). This could lead to an overstatement in the benefit of the climate action if this is not considered (if detected contrails are treated as the only contrails), or at least extrapolation based on a smaller observable fraction. Contrail observability should be considered when assessing

525 any action on emissions or contrail mitigation.

This work can be expanded to consider meteorological conditions—particularly contrail overlap with underlying cloud and contrail outbreaks—as an obstacle to observability. Observation away from the sub-satellite region has also been neglected. The impact of this effect is not straightforward. A higher viewing zenith angle reduces the effective resolution, reducing contrail observability assuming the same contrail properties and meteorology. However, the longer atmospheric path length

530 will enhance the effective cloud optical depth, making thinner contrails easier to detect (Maddux et al., 2010). Additionally, more-physical atmospheric profiles may impact the brightness temperature fields observed. Granularity in aircraft and engine properties stands to be considered, beyond the simple fuel case examined here.

Nonetheless, this work should give confidence to the use of contrail observations using satellites—under best-case conditions, the most radiatively important contrails are strongly observable.

535 *Code and data availability.* CoCiP data is from Teoh et al. (2023), which details input data sources. Radiative transfer code uses libRadtran (Emde et al., 2016) and pyLRT (Gryspeerdt and Driver, 2024). The contrail detection algorithm is adapted based on code released with McCloskey et al. (2021).

Author contributions. All the authors contributed to designing the study. OD performed the analysis and wrote the manuscript. EG and MS provided comments and suggestions.

540 *Competing interests.* The authors have no competing interests to declare.

Acknowledgements. This work has received funding from a Royal Society University Research Fellowship (URF/R1/191602) and the EP-SRC Centre for Doctoral Training in Aerosol Science (EP/S023593/1).

We thank Roger Teoh (Imperial College London) and Zebediah Engburg (Breakthrough Energy), who provided access to global CoCiP data output for both Jet-A1 fuel and with modelled SAF adoption.

References

Agarwal, A., Meijer, V. R., Eastham, S. D., Speth, R. L., and Barrett, S. R. H.: Reanalysis-Driven Simulations May Overestimate Persistent Contrail Formation by 100%–250%, Environmental Research Letters, 17, 014 045, https://doi.org/10.1088/1748-9326/ac38d9, 2022.

Bakan, S., Betancor, M., Gayler, V., and Graßl, H.: Contrail Frequency over Europe from NOAA-satellite Images, Annales Geophysicae, 12, 962–968, https://doi.org/10.1007/s00585-994-0962-y, 1994.

Bodas-Salcedo, A., Webb, M. J., Bony, S., Chepfer, H., Dufresne, J.-L., Klein, S. A., Zhang, Y., Marchand, R., Haynes, J. M., Pincus, R., and John, V. O.: COSP: Satellite Simulation Software for Model Assessment, Bulletin of the American Meteorological Society, 92, 1023–1043, https://doi.org/10.1175/2011BAMS2856.1, 2011.

Buras, R., Dowling, T., and Emde, C.: New Secondary-Scattering Correction in DISORT with Increased Efficiency for Forward Scattering, Journal of Quantitative Spectroscopy and Radiative Transfer, 112, 2028–2034, https://doi.org/10.1016/j.jqsrt.2011.03.019, 2011.

Chevallier, R., Shapiro, M., Engberg, Z., Soler, M., and Delahaye, D.: Linear Contrails Detection, Tracking and Matching with Aircraft Using Geostationary Satellite and Air Traffic Data, Aerospace, 10, 578, https://doi.org/10.3390/aerospace10070578, 2023.

Cornet, C., C-Labonnote, L., and Szczap, F.: Three-Dimensional Polarized Monte Carlo Atmospheric Radiative Transfer Model (3DM-CPOL): 3D Effects on Polarized Visible Reflectances of a Cirrus Cloud, Journal of Quantitative Spectroscopy and Radiative Transfer, 111, 174–186, https://doi.org/10.1016/j.jqsrt.2009.06.013, 2010.

Duda, D. P., Minnis, P., Khlopenkov, K., Chee, T. L., and Boeke, R.: Estimation of 2006 Northern Hemisphere Contrail Coverage Using MODIS Data: ESTIMATION OF 2006 NH CONTRAIL COVERAGE, Geophysical Research Letters, 40, 612–617, https://doi.org/10.1002/grl.50097, 2013.

Emde, C., Buras-Schnell, R., Kylling, A., Mayer, B., Gasteiger, J., Hamann, U., Kylling, J., Richter, B., Pause, C., Dowling, T., and Bugliaro, L.: The libRadtran Software Package for Radiative Transfer Calculations (Version 2.0.1), Geoscientific Model Development, 9, 1647–1672, https://doi.org/10.5194/gmd-9-1647-2016, 2016.

Gasteiger, J., Emde, C., Mayer, B., Buras, R., Buehler, S. A., and Lemke, O.: Representative Wavelengths Absorption Parameterization Applied to Satellite Channels and Spectral Bands, Journal of Quantitative Spectroscopy and Radiative Transfer, 148, 99–115, https://doi.org/10.1016/j.jqsrt.2014.06.024, 2014.

Geraedts, S., Brand, E., Dean, T. R., Eastham, S., Elkin, C., Engberg, Z., Hager, U., Langmore, I., McCloskey, K., Ng, J. Y.-H., Platt, J. C., Sankar, T., Sarna, A., Shapiro, M., and Goyal, N.: A Scalable System to Measure Contrail Formation on a Per-Flight Basis, https://doi.org/10.48550/arXiv.2308.02707, 2023.

Gierens, K. and Vázquez-Navarro, M.: Statistical Analysis of Contrail Lifetimes from a Satellite Perspective, Meteorologische Zeitschrift, 27, 183–193, https://doi.org/10.1127/metz/2018/0888, 2018.

Gierens, K., Matthes, S., and Rohs, S.: How Well Can Persistent Contrails Be Predicted?, Aerospace, 7, 169, https://doi.org/10.3390/aerospace7120169, 2020.

Gryspeerdt, E. and Driver, O.: pyLRT, Zenodo, https://doi.org/10.5281/zenodo.11626012, 2024.

Gryspeerdt, E., Stettler, M. E. J., Teoh, R., Burkhardt, U., Delovski, T., Driver, O. G. A., and Painemal, D.: Operational Differences Lead to Longer Lifetimes of Satellite Detectable Contrails from More Fuel Efficient Aircraft, 2024.

Jeßberger, P., Voigt, C., Schumann, U., Sölch, I., Schlager, H., Kaufmann, S., Petzold, A., Schäuble, D., and Gayet, J.-F.: Aircraft Type Influence on Contrail Properties, Atmospheric Chemistry and Physics, 13, 11 965–11 984, https://doi.org/10.5194/acp-13-11965-2013, 2013.

Kärcher, B.: Formation and Radiative Forcing of Contrail Cirrus, Nature Communications, 9, 1824, https://doi.org/10.1038/s41467-018-04068-0, 2018.

Kärcher, B., Burkhardt, U., Unterstrasser, S., and Minnis, P.: Factors Controlling Contrail Cirrus Optical Depth, Atmospheric Chemistry and Physics, 9, 6229–6254, https://doi.org/10.5194/acp-9-6229-2009, 2009.

Lee, D., Fahey, D., Skowron, A., Allen, M., Burkhardt, U., Chen, Q., Doherty, S., Freeman, S., Forster, P., Fuglestvedt, J., Gettelman, A., De León, R., Lim, L., Lund, M., Millar, R., Owen, B., Penner, J., Pitari, G., Prather, M., Sausen, R., and Wilcox, L.: The Contribution of Global Aviation to Anthropogenic Climate Forcing for 2000 to 2018, Atmospheric Environment, 244, 117 834, https://doi.org/10.1016/j.atmosenv.2020.117834, 2021.

Lee, T. F.: Jet Contrail Identification Using the AVI-IRR Infrared Split Window, Journal of Applied Meteorology and Climatology, 28, 993–995, https://doi.org/10.1175/1520-0450(1989)028<0993:JCIUTA>2.0.CO;2, 1989.

Lever, J., Krzywinski, M., and Altman, N.: Principal Component Analysis, Nature Methods, 14, 641–642, https://doi.org/10.1038/nmeth.4346, 2017.

Maddux, B. C., Ackerman, S. A., and Platnick, S.: Viewing Geometry Dependencies in MODIS Cloud Products, Journal of Atmospheric and Oceanic Technology, 27, 1519–1528, https://doi.org/10.1175/2010JTECHA1432.1, 2010.

Mannstein, H., Meyer, R., and Wendling, P.: Operational Detection of Contrails from NOAA-AVHRR-data, International Journal of Remote Sensing, 20, 1641–1660, https://doi.org/10.1080/014311699212650, 1999.

McCloskey, K. J. F., Geraedts, S. D., Jackman, B. H., Meijer, V. R., Brand, E. W., Fork, D. K., Platt, J., Elkin, C., and Arsdale, C. H. V.: A Human-Labeled Landsat Contrails Dataset, 2021.

Meerkötter, R., Schumann, U., Doelling, D. R., Minnis, P., Nakajima, T., and Tsushima, Y.: Radiative Forcing by Contrails, Annales Geophysicae, 17, 1080–1094, https://doi.org/10.1007/s00585-999-1080-7, 1999.

Meijer, V. R., Kulik, L., Eastham, S. D., Allroggen, F., Speth, R. L., Karaman, S., and Barrett, S. R. H.: Contrail Coverage over the United States before and during the COVID-19 Pandemic, Environmental Research Letters, 17, 034 039, https://doi.org/10.1088/1748-9326/ac26f0, 2022.

Meyer, R., Mannstein, H., Meerkötter, R., Schumann, U., and Wendling, P.: Regional Radiative Forcing by Line-Shaped Contrails Derived from Satellite Data: CONTRAIL RADIATIVE FORCING FROM SATELLITE DATA, Journal of Geophysical Research: Atmospheres, 107, ACL 17–1–ACL 17–15, https://doi.org/10.1029/2001JD000426, 2002.

Meyer, R., Buell, R., Leiter, C., Mannstein, H., Pechtl, S., Oki, T., and Wendling, P.: Contrail Observations over Southern and Eastern Asia in NOAA/AVHRR Data and Comparisons to Contrail Simulations in a GCM, International Journal of Remote Sensing, 28, 2049–2069, https://doi.org/10.1080/01431160600641707, 2007.

Minnis, P., Palikonda, R., Walter, B., Ayers, J., and Mannstein, H.: Contrail Properties over the Eastern North Pacific from AVHRR Data, Meteorologische Zeitschrift, 14, 515–523, https://doi.org/10.1127/0941-2948/2005/0056, 2005.

Molloy, J., Teoh, R., Harty, S., Koudis, G., Schumann, U., Poll, I., and Stettler, M. E. J.: Design Principles for a Contrail-Minimizing Trial in the North Atlantic, Aerospace, 9, 375, https://doi.org/10.3390/aerospace9070375, 2022.

Ng, J. Y.-H., McCloskey, K., Cui, J., Brand, E., Sarna, A., Goyal, N., Van Arsdale, C., and Geraedts, S.: OpenContrails: Benchmarking Contrail Detection on GOES-16 ABI, http://arxiv.org/abs/2304.02122, 2023.

NOAA: GOES-R Series Data Book, https://www.goes-r.gov/downloads/resources/documents/GOES-RSeriesDataBook.pdf, 2019.

Palikonda, R., Minnis, P., Duda, D. P., and Mannstein, H.: Contrail Coverage Derived from 2001 AVHRR Data over the Continental United States of America and Surrounding Areas, Meteorologische Zeitschrift, 14, 525–536, https://doi.org/10.1127/0941-2948/2005/0051, 2005.

620 Ponsonby, J., King, L., Murray, B. J., and Stettler, M. E. J.: Jet Aircraft Lubrication Oil Droplets as Contrail Ice-Forming Particles, Atmospheric Chemistry and Physics, 24, 2045–2058, https://doi.org/10.5194/acp-24-2045-2024, 2024.

Sausen, R., Hofer, S., Gierens, K., Bugliaro, L., Ehrmanntraut, R., Sitova, I., Walczak, K., Burridge-Diesing, A., Bowman, M., and Miller, N.: Can We Successfully Avoid Persistent Contrails by Small Altitude Adjustments of Flights in the Real World?, Meteorologische Zeitschrift, https://doi.org/10.1127/metz/2023/1157, 2023.

625 Schumann, U.: On Conditions for Contrail Formation from Aircraft Exhausts, Meteorologische Zeitschrift, 5, 4–23, https://doi.org/10.1127/metz/5/1996/4, 1996.

Schumann, U.: A Contrail Cirrus Prediction Model, Geoscientific Model Development, 5, 543–580, https://doi.org/10.5194/gmd-5-543-2012, 2012.

Schumann, U. and Heymsfield, A. J.: On the Life Cycle of Individual Contrails and Contrail Cirrus, Meteorological Monographs, 58, 3.1–
630 3.24, https://doi.org/10.1175/AMSMONOGRAPHS-D-16-0005.1, 2017.

Schumann, U., Mayer, B., Graf, K., and Mannstein, H.: A Parametric Radiative Forcing Model for Contrail Cirrus, Journal of Applied Meteorology and Climatology, 51, 1391–1406, https://doi.org/10.1175/JAMC-D-11-0242.1, 2012.

Schumann, U., Penner, J. E., Chen, Y., Zhou, C., and Graf, K.: Dehydration Effects from Contrails in a Coupled Contrail–Climate Model, Atmospheric Chemistry and Physics, 15, 11 179–11 199, https://doi.org/10.5194/acp-15-11179-2015, 2015.

635 Schumann, U., Baumann, R., Baumgardner, D., Bedka, S. T., Duda, D. P., Freudenthaler, V., Gayet, J.-F., Heymsfield, A. J., Minnis, P., Quante, M., Raschke, E., Schlager, H., Vázquez-Navarro, M., Voigt, C., and Wang, Z.: Properties of Individual Contrails: A Compilation of Observations and Some Comparisons, Atmospheric Chemistry and Physics, 17, 403–438, https://doi.org/10.5194/acp-17-403-2017, 2017.

Shapiro, M., Engberg, Z., Teoh, R., Stettler, M., and Dean, T.: Pycontrails: Python Library for Modeling Aviation Climate Impacts, Zenodo,
640 https://doi.org/10.5281/zenodo.10182539, 2023.

Shenk, W. E. and Salomonson, V. V.: A Simulation Study Exploring the Effects of Sensor Spatial Resolution on Estimates of Cloud Cover from Satellites, https://journals.ametsoc.org/view/journals/apme/11/1/1520-0450_1972_011_0214_assete_2_0_co_2.xml, 1972.

Teoh, R., Schumann, U., Majumdar, A., and Stettler, M. E. J.: Mitigating the Climate Forcing of Aircraft Contrails by Small-Scale Diversions and Technology Adoption, Environmental Science & Technology, 54, 2941–2950, https://doi.org/10.1021/acs.est.9b05608, 2020.

645 Teoh, R., Schumann, U., Gryspeerdt, E., Shapiro, M., Molloy, J., Koudis, G., Voigt, C., and Stettler, M. E. J.: Aviation Contrail Climate Effects in the North Atlantic from 2016 to 2021, Atmospheric Chemistry and Physics, 22, 10 919–10 935, https://doi.org/10.5194/acp-22-10919-2022, 2022a.

Teoh, R., Schumann, U., Voigt, C., Schripp, T., Shapiro, M., Engberg, Z., Molloy, J., Koudis, G., and Stettler, M. E. J.: Targeted Use of Sustainable Aviation Fuel to Maximize Climate Benefits, Environmental Science & Technology, 56, 17 246–17 255,
650 https://doi.org/10.1021/acs.est.2c05781, 2022b.

Teoh, R., Engberg, Z., Schumann, U., Voigt, C., Shapiro, M., Rohs, S., and Stettler, M.: Global Aviation Contrail Climate Effects from 2019 to 2021, EGUsphere, pp. 1–32, https://doi.org/10.5194/egusphere-2023-1859, 2023.

Vázquez-Navarro, M., Mannstein, H., and Kox, S.: Contrail Life Cycle and Properties from 1 Year of MSG/SEVIRI Rapid-Scan Images, Atmospheric Chemistry and Physics, 15, 8739–8749, https://doi.org/10.5194/acp-15-8739-2015, 2015.

655 Voigt, C., Schumann, U., Minikin, A., Abdelmonem, A., Afchine, A., Borrmann, S., Boettcher, M., Buchholz, B., Bugliaro, L., Costa, A., Curtius, J., Dollner, M., Dörnbrack, A., Dreiling, V., Ebert, V., Ehrlich, A., Fix, A., Forster, L., Frank, F., Fütterer, D., Giez, A., Graf, K., Grooß, J.-U., Groß, S., Heimerl, K., Heinold, B., Hüneke, T., Järvinen, E., Jurkat, T., Kaufmann, S., Kenntner, M., Klingebiel, M.,

Klimach, T., Kohl, R., Krämer, M., Krisna, T. C., Luebke, A., Mayer, B., Mertes, S., Molleker, S., Petzold, A., Pfeilsticker, K., Port, M., Rapp, M., Reutter, P., Rolf, C., Rose, D., Sauer, D., Schäfler, A., Schlage, R., Schnaiter, M., Schneider, J., Spelten, N., Spichtinger, P.,

660   Stock, P., Walser, A., Weigel, R., Weinzierl, B., Wendisch, M., Werner, F., Wernli, H., Wirth, M., Zahn, A., Ziereis, H., and Zöger, M.: ML-CIRRUS: The Airborne Experiment on Natural Cirrus and Contrail Cirrus with the High-Altitude Long-Range Research Aircraft HALO, Bulletin of the American Meteorological Society, 98, 271–288, https://doi.org/10.1175/BAMS-D-15-00213.1, 2017.

Voigt, C., Kleine, J., Sauer, D., Moore, R. H., Bräuer, T., Le Clercq, P., Kaufmann, S., Scheibe, M., Jurkat-Witschas, T., Aigner, M., Bauder, U., Boose, Y., Borrmann, S., Crosbie, E., Diskin, G. S., DiGangi, J., Hahn, V., Heckl, C., Huber, F., Nowak, J. B., Rapp, M., Rauch, B.,

665   Robinson, C., Schripp, T., Shook, M., Winstead, E., Ziemba, L., Schlager, H., and Anderson, B. E.: Cleaner Burning Aviation Fuels Can Reduce Contrail Cloudiness, Communications Earth & Environment, 2, 1–10, https://doi.org/10.1038/s43247-021-00174-y, 2021.

Wu, X. and Schmidt, T.: GOES-16 ABI Level 1b and Cloud and Moisture Imagery (CMI) Release Full Validation Data Quality Product Performance Guide for Data Users, 2019.

Yang, P., Hong, G., Dessler, A. E., Ou, S. S. C., Liou, K.-N., Minnis, P., and Harshvardhan: Contrails and Induced Cirrus: Optics and

670   Radiation, Bulletin of the American Meteorological Society, 91, 473–478, https://doi.org/10.1175/2009BAMS2837.1, 2010.

Yang, P., Bi, L., Baum, B. A., Liou, K.-N., Kattawar, G. W., Mishchenko, M. I., and Cole, B.: Spectrally Consistent Scattering, Absorption, and Polarization Properties of Atmospheric Ice Crystals at Wavelengths from 0.2 to 100 Mm, Journal of the Atmospheric Sciences, 70, 330–347, https://doi.org/10.1175/JAS-D-12-039.1, 2013.

Zhang, G., Zhang, J., and Shang, J.: Contrail Recognition with Convolutional Neural Network and Contrail Parameterizations Evaluation,

675   Sola, 14, 132–137, https://doi.org/10.2151/sola.2018-023, 2018.